Eur. Phys. J. C (2014) 74:2823
DOI 10.1140/epjc/s10052-014-2823-5

THE EUROPEAN PHYSICAL JOURNAL C

Regular Article - Theoretical Physics

Precise photoproduction of the charged top-pions at the LHC with forward detector acceptances

Hao Sun[1,3,a], **Chong-Xing Yue**[2,b]

[1] Department of Physics, Dalian University of Technology, Dalian 116024, People's Republic of China
[2] Department of Physics, Liaoning Normal University, Dalian 116029, People's Republic of China
[3] School of Physics and Technology, University of Jinan, Jinan 250022, People's Republic of China

Received: 29 October 2013 / Accepted: 14 March 2014 / Published online: 9 April 2014

Abstract We study the photoproduction of the charged top-pion predicted by the top triangle moose (TTM) model (a deconstructed version of the topcolor-assisted technicolor TC2 model) via the processes $pp \to p\gamma p \to \pi_t^{\pm} t + X$ at the 14 TeV Large Hadron Collider (LHC) including next-to-leading order (NLO) QCD corrections. Our results show that the production cross sections and distributions are sensitive to the free parameters $\sin\omega$ and M_{π_t}. A typical QCD correction value is $7-11$ % and this does not depend much on $\sin\omega$ as well as the forward detector acceptances.

1 Introduction

The top quark is the heaviest known elementary particle, which makes it an excellent candidate for new physics searches. The origin of its mass might be different from that of the other quarks and leptons; a top quark condensate ($\langle t\bar{t}\rangle$), for example, could be responsible for at least part of the mechanism of electroweak symmetry breaking (EWSB). An interesting model involving a role for the top quark in dynamical EWSB is known as the topcolor-assisted technicolor (TC2) model [1–3]. Higgsless models [4] have emerged as a novel way of understanding the mechanism of EWSB without the presence of a scalar particle in the spectrum. Recently, combing Higgsless and topcolor mechanisms, a deconstructed Higgsless model was proposed, called the top triangle moose (TTM) model [5,6]. In this model, EWSB results largely from the Higgsless mechanism, while the top quark mass is mainly generated by the topcolor mechanism. The TTM model alleviates the tension between obtaining the correct top quark mass and keeping $\Delta\rho$ small that exists in many Higgsless models, which can be seen as the deconstructed version of the TC2 model. The new physics models belonging to the topcolor scenario generically have two sources of EWSB and there are two sets of Goldstone bosons. One set is eaten by the electroweak (EW) gauge bosons W and Z to generate their masses, while the other set remains in the spectrum, which is called the top-pions (π_t^0 and $\pi_t^{\pm}$). The topcolor scenario also predicts the existence of the top-Higgs h_t^0, which is the $t\bar{t}$ bound state. The possible signals of these new scalar particles have been extensively studied in the literature, however, most studies have been done in the context of the TC2 model. A phenomenological analysis of the top-pions and top-Higgs predicted by the TTM model [5–7] is necessary.

The Large Hadron Collider (LHC) generates high-energetic proton–proton (pp) collisions with a luminosity of $\mathcal{L} = 10^{34}\ \mathrm{cm}^{-2}\ \mathrm{s}^{-1}$. It provides high statistics data at high energies. On the other hand hadronic interactions generally involve serious backgrounds. A new phenomenon called exclusive production was observed in the measurements of CDF collaboration including exclusive lepton pair production [8,9], photon–photon production [10], dijet production [11], exclusive charmonium (J/ψ) meson photoproduction [12], etc. Complementary to pp interactions, studies of exclusive production of leptons, photons, and heavy particles might be possible and this opens a new field of studying very high-energy photon–photon ($\gamma\gamma$) and photon–proton (γp) interactions.

Following the experience from HERA and the Tevatron, new detectors are proposed to be installed in the LHC tunnel as an additional upgrade of the ATLAS and CMS detectors. There is a program of studying forward physics with extra detectors located in a region nearly 100–400 m from the interaction point [13–17]. Technical details of the ATLAS Forward Physics (AFP) projects can be found, for example, in Ref. [18]. This forward detector equipment allows one to detect intact scattered protons after the collision. There-

[a] e-mail: haosun@mail.ustc.edu.cn; haosun@dlut.edu.cn
[b] e-mail: cxyue@lnnu.edu.cn

fore the processes which spoil the proton structure can easily be discerned from the exclusive photoproduction processes. By the use of forward detector equipment we can eliminate many serious backgrounds. This is one of the advantages of exclusive photoproduction processes.

A brief review of the experimental prospects for studying high-energy $\gamma\gamma$ and γp interactions is discussed in Ref. [19] and cross sections are calculated for many EW and BSM processes. Many phenomenological studies of photon-produced processes are summarized here, involving: standard model productions [20–22], supersymmetry [23–28], extra dimensions [29–31], unparticle physics [32], gauge boson self-interactions [33–42], neutrino electromagnetic properties [43–45], top quark physics [21,22,46–48], and triplet Higgs production [49], etc.

Photoproduction of the charged top-pion at leading order (LO) has been studied in Refs. [50,51], which proceeds via the subprocess $\gamma c \to \pi_t^{\pm} b$ mediated by the flavor changing couplings and through $\gamma b \to \pi_t^{\pm} t$ at the large hadron–electron collider (LHeC) [52]. At the LHC, in a general pp collision, the charged top-pion can be produced in association with a top quark through bottom–gluon fusion, $gb \to t\pi_t^-$, and through gluon–gluon fusion, $gg \to \bar{b}t\pi_t^-$, phenomenologically similar to a charged Higgs boson in a two-Higgs-doublet model with low $\tan\beta$. A related NLO study can be found in Ref. [53]. On the other hand, $\pi_t^{\pm}\, t$ associated production at the γp collision LHC will be very clean or at least with backgrounds easy going, thus leading to a good chance to be detected. It can be a complementary process to be studied in addition of $gb \to t\pi_t^-$. In this paper, we present this production at the γp collision assuming a typical LHC multipurpose forward detector. Accurate theoretical predictions including higher order QCD corrections are included. This paper is organized as follows: in Sect. 2 we present a brief introduction to the calculation framework including the TTM model description, EPA implementation, and LO and NLO cross section calculations. Section 3 is arranged to present numerical checks and results of our studies. Finally we summarize the conclusions in the last section.

2 Calculation framework

2.1 The essential features of the TTM model

The detailed description of the TTM model can be found in Refs. [5,6], and here we just briefly review its essential features which are related to our calculation. The EW gauge structure of the TTM model is $SU(2)_0 \times SU(2)_1 \times U(1)_2$. The nonlinear sigma field $\sum_{01}$ breaks the group $SU(2)_0 \times SU(2)_1$ down to $SU(2)$ and field $\sum_{12}$ breaks $SU(2)_1 \times U(1)_2$ down to $U(1)$. To separate top-quark mass generation from EWSB, a top-Higgs field Φ is introduced to the TTM model, which couples preferentially to the top quark. To ensure that most of EWSB comes from the Higgsless side, the VEVs of the fields $\sum_{01}$ and $\sum_{12}$ are chosen to be $\langle\sum_{01}\rangle = \langle\sum_{12}\rangle = F = \sqrt{2}v\cos\omega$, in which $v = 246$ GeV is the EW scale and ω is a new small parameter. The VEV of the top-Higgs field is $f = \langle\Phi\rangle = v\sin\omega$.

From the above discussions, we can see that, for the TTM model, there are six scalar degrees of freedom on the Higgsless sector and four on the top-Higgs sector. Six of these Goldstone bosons are eaten to give masses to the gauge bosons $W^{\pm}$, Z, $W'^{\pm}$ and Z'. The others remain as physical states in the spectrum, which are called top-pions ($\pi_t^{\pm}$ and π_t^0) and top-Higgs (h_t^0). In this paper, we will focus our attention on photoproduction of the charged top-pions via γp collisions at the LHC. The couplings of the charged top-pions $\pi_t^{\pm}$ to ordinary particles, which are related to our calculation, are given by Ref. [6]:

$$\mathcal{L}_{\pi_t tb} = i\lambda_t \cos\omega \left\{1 - \frac{x^2[a^4 + (a^4 - 2a^2 + 2)\cos 2\omega]}{8(a^2-1)^2}\right\} \times \pi_t^+ \bar{t}_R b_L + \text{h.c.}, \tag{1}$$

with

$$\lambda_t = \frac{\sqrt{2}m_t}{v\sin\omega}\left[\frac{M_D^2(\varepsilon_L^2+1) - m_t^2}{M_D^2 - m_t^2}\right],$$
$$a = \frac{v\sin\omega}{\sqrt{2}M_D}, \quad x = \sqrt{2}\varepsilon_L = \frac{2\cos\omega M_W}{M_{W'}}. \tag{2}$$

Here we assume the CKM matrix to be the identity and we omit the light quark masses. M_D is the mass scale of the heavy fermion and $M_{W'}$ is the mass of the new gauge boson W'. Since the top quark mass depends very little on the right-handed delocalization parameter ε_{tR}, we have set $\varepsilon_{tR} = 0$ in Eq. (1). The parameter ε_L describes the degree of delocalization of the left-handed fermions and is flavor universal, the parameter x represents the ratio of the gauge couplings. The relationship between ε_L and x, which is given in Eq. (2), is imposed by ideal delocalization.

Reference [54] has shown that $M_{W'}$ should be larger than 380 GeV, as demanded by the LEPII data and smaller than 1.2 TeV by the need to maintain perturbative unitarity in $W_L W_L$ scattering. It is obvious that the coupling $\pi_t tb$ is not very sensitive to the parameters $M_{W'}$ and M_D. Thus, the production cross sections of the subprocesses $\gamma b \to t\pi_t^-$ and $\gamma\bar{b} \to \bar{t}\pi_t^+$ are not strongly dependent on the values of the mass parameters $M_{W'}$ and M_D. In our following numerical calculation, we will take the illustrative values $M_{W'} = 500$ GeV and $M_D = 400$ GeV. In this case, we have $[M_D^2(\varepsilon_L^2+1) - m_t^2]/(M_D^2 - m_t^2) \approx 1$ and Eq. (1) can be approximately written as

$$\mathcal{L}_{\pi_t tb} \approx i\frac{\sqrt{2}m_t C}{v}\cot\omega\pi_t^+\bar{t}_R b_L + \text{h.c.} \tag{3}$$

with

$$C = 1 - \frac{x^2[a^4 + (a^4 - 2a^2 + 2)\cos 2\omega]}{8(a^2-1)^2}. \quad (4)$$

It is obvious that the constant C is not sensitive to the value of $\sin\omega$ and its value is close to 1. The parameter $\sin\omega$ indicates the fraction of EWSB provided by the top condensate. The top-pion mass M_{π_t} depends on the amount of top-quark mass arising from the extended technicolor (ETC) sector and on the effects of EW gauge interactions [55,56], and thus its value is model-dependent. In the context of the TTM model, Ref. [6] has obtained the constraints on the top-pion mass via studying its effects on the relevant experimental observables. Similarly to Refs. [6,57], we will assume it as a free parameter.

2.2 Equivalent photon approximation (EPA)

In γp collisions, the quasi-real photons are emitted from protons with very low virtuality so that it is a good approximation to assume that they are on-mass-shell. These quasi-real photons are scattered with small angles and low transverse momentum. At the same time, protons emitting photons remain intact and are not spoilt. Intact protons thus deviate slightly from their trajectory along the beam path without being detected by central detectors. Deflected protons and their energy loss will be detected by the forward detectors with a very large pseudorapidity. Photons emitted with small angles by the protons show a spectrum of virtuality Q^2 and energy E_γ. This is described by the equivalent photon approximation (EPA) [58–60], which differs from the point-like electron (positron) case by taking care of the electromagnetic form factors in the equivalent γ spectrum and effective γ luminosity:

$$\frac{\mathrm{d}N_\gamma}{\mathrm{d}E_\gamma \mathrm{d}Q^2} = \frac{\alpha}{\pi}\frac{1}{E_\gamma Q^2}\left[\left(1-\frac{E_\gamma}{E}\right)\left(1-\frac{Q^2_{min}}{Q^2}\right)F_E + \frac{E_\gamma^2}{2E^2}F_M\right] \quad (5)$$

with

$$Q^2_{\min} = \frac{M_p^2 E_\gamma^2}{E(E-E_\gamma)}, \quad F_E = \frac{4M_p^2 G_E^2 + Q^2 G_M^2}{4M_p^2 + Q^2},$$

$$G_E^2 = \frac{G_M^2}{\mu_p^2} = \left(1+\frac{Q^2}{Q_0^2}\right)^{-4}, \quad F_M = G_M^2, \quad Q_0^2 = 0.71\ \mathrm{GeV}^2,$$

where α is the fine-structure constant, E is the energy of the incoming proton beam, which is related to the quasi-real photon energy by $E_\gamma = \xi E$, and M_p is the mass of the proton. $\xi = (|p| - |p'|)/|p|$, where p and p' are the momenta of incoming protons and intact scattered protons, respectively. $\mu_p^2 = 7.78$ is the magnetic moment of the proton. F_E and F_M are functions of the electric and magnetic form factors. In this case, if both incoming emitted protons remain intact, that provides the $\gamma\gamma$ collision and it can be cleaner than the γp collision; however, γp collisions have higher energy and effective luminosity with respect to $\gamma\gamma$ interactions.

2.3 The cross sections up to NLO

We denote the parton level process as $\gamma(p_1)b(p_2) \to \pi_t^\pm(p_3)t(p_4)$ where p_i are the particle four momenta. The hadronic cross section at the LHC can be converted by integrating $\gamma b \to \pi_t^\pm t$ over the photon ($\mathrm{d}N(x, Q^2)$) and quark ($G_{b/p}(x_2, \mu_f)$) spectra:

$$\sigma = \int_{\frac{M_{inv}}{\sqrt{s}}}^{\sqrt{\xi_{max}}} 2z\,\mathrm{d}z \int_{\mathrm{Max}(z^2,\xi_{\min})}^{\xi_{\max}} \frac{\mathrm{d}x_1}{x_1} \int_{Q^2_{\min}}^{Q^2_{\max}} \frac{\mathrm{d}N_\gamma(x_1)}{\mathrm{d}x_1 \mathrm{d}Q^2} G_{b/p}\left(\frac{z^2}{x_1}, \mu_f\right) \cdot \int \frac{1}{\mathrm{avgfac}} \frac{|\mathcal{M}_n(\hat{s}=z^2 s)|^2}{2\hat{s}(2\pi)^{3n-4}}\,\mathrm{d}\Phi_n, \quad (6)$$

where x_1 is the ratio between scattered quasi-real photons and incoming proton energy $x_1 = E_\gamma/E$ and x_2 is the momentum fraction of the protons momentum carried by the bottom quark. The quantity $\hat{s} = z^2 s$ is the effective c.m.s. energy with $z^2 = x_1 x_2$. M_{inv} being the total mass of the $\pi_t^\pm t$ final state. $\frac{2z}{x_1}$ is the Jacobian determinant for transforming the differentials from $\mathrm{d}x_1\mathrm{d}x_2$ into $\mathrm{d}x_1\mathrm{d}z$. $G_{b/p}(x, \mu_f)$ represent the bottom quark parton density functions, μ_f is the factorization scale, which can be chosen equal to the renormalization scale μ_r when the loop calculation is included. $\frac{1}{\mathrm{avgfac}}$ is the spin-average factor, color-average factor, and identical particle factor. $|\mathcal{M}_n|^2$ represents the squared n-particle matrix element and is divided by the flux factor $[2\hat{s}(2\pi)^{3n-4}]$. $\mathrm{d}\Phi_n$ is the n-body phase space differential.

The parton Feynman diagrams at tree level are shown in Fig. 1a, b. We only consider the $\pi_t^- t$ production while its charge-conjugate contribution is the same. At NLO QCD loop level, the Feynman diagrams are presented in Figs. 2 and 3, corresponding to loop (σ^{loop}) and real (σ^{real}) contributions, respectively. There exist ultraviolet (UV) and soft/collinear IR singularities in σ^{loop}. To remove the UV divergences, we introduce the wave function renormalization constants $\delta Z_{\psi_{q,L,R}}$ for massless bottom and massive top

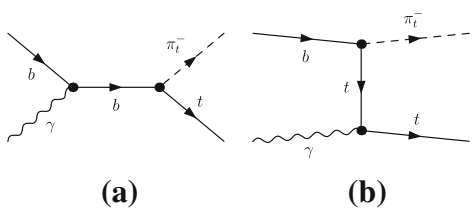

Fig. 1 Tree parton level Feynman diagrams for $rb \to \pi_t^- t$ in the TTM frame

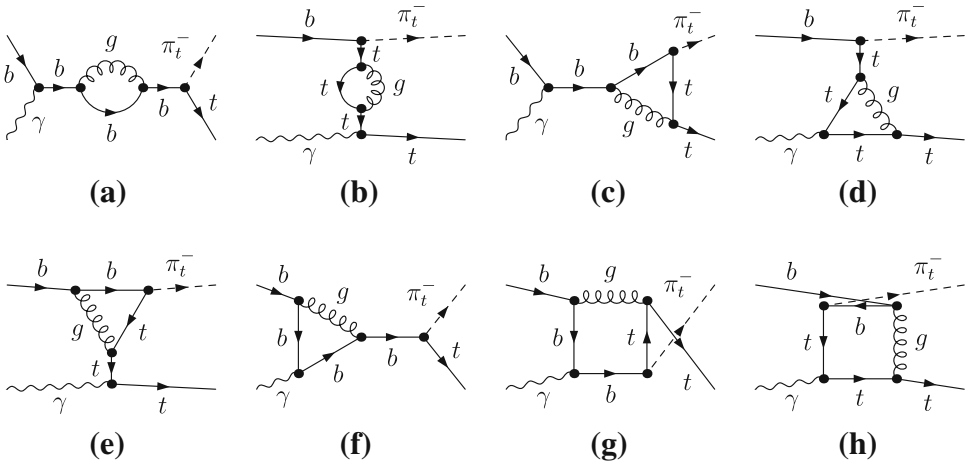

Fig. 2 The QCD one-loop Feynman diagrams for the partonic process $\gamma b \to \pi_t^- t$ (**a**–**h**). Counterterm diagrams corresponding to Fig. 1 are not shown here

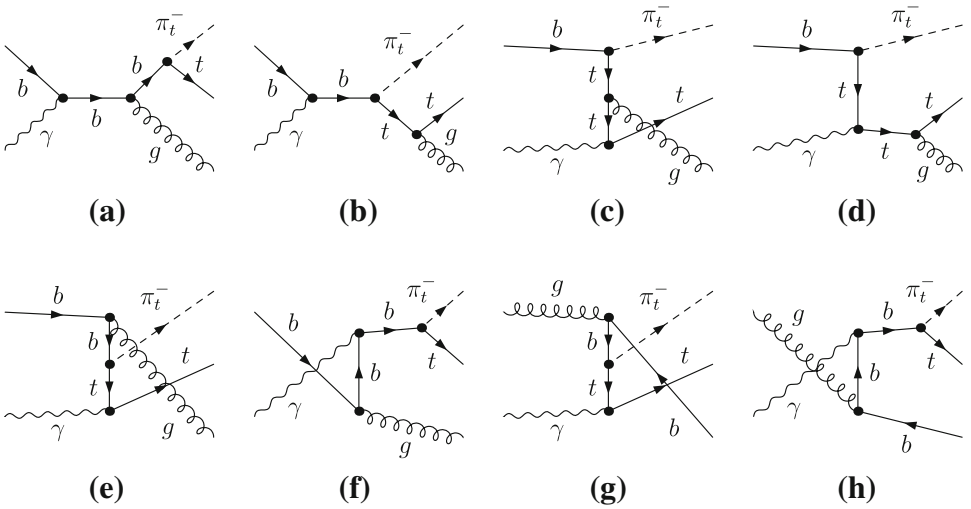

Fig. 3 Some the tree level Feynman diagrams for the real gluon/light-(anti)quark emission subprocess $\gamma b \to \pi_t^- tg$ related to the first process in Eq. 7 (**a**–**f**) and $\gamma g \to \pi_t^- t\bar{b}$ related to the second process in Eq. 7 (**g**, **h**)

fields as $\psi^0_{q,L,R} = (1 + \delta Z_{\phi_{q,L,R}})^{\frac{1}{2}} \psi_{q,L,R}$. In the modified minimal subtraction ($\overline{MS}$) renormalization scheme the renormalization constants for the massless quarks, and massive top quark (defined on shell) are expressed as $\delta Z_{\psi_{q,L}} = -\frac{\alpha_s}{4\pi} C_F(\Delta_{\rm UV} - \Delta_{\rm IR})$, $\delta Z_{\psi_{q,R}} = -\frac{\alpha_s}{4\pi} C_F(\Delta_{\rm UV} - \Delta_{\rm IR})$ and $\frac{\delta m_t}{m_t} = -\frac{\alpha_s}{3\pi}[3\Delta_{\rm UV} + 4]$, with $C_F = \frac{4}{3}$. $\Delta_{\rm UV,IR} = \frac{1}{\epsilon_{\rm UV,IR}} \Gamma(1 + \epsilon_{\rm UV,IR})(4\pi)^{\epsilon_{\rm UV,IR}}$ referring to the UV and IR divergences, respectively. By adding a renormalization part to the virtual corrections, any UV singularities are regulated leaving soft/collinear IR singularities untouched. These IR singularities will be removed by combining the real emission corrections. Singularities associated with initial state collinear gluon emission are absorbed into the definition of the parton distribution functions. We employ the $\overline{MS}$ scheme for the parton distribution functions. Similar to the virtual part, we utilize dimensional regularization to control the singularities of the radiative corrections, which are organized using the two cutoff phase space slicing (TCPSS) method [61]. We adopt TCPSS to isolate the IR singularities by introducing two cutoff parameters δ_s and δ_c. An arbitrary small δ_s separates the three-body final state phase space into two regions: the soft region ($E_5 \le \delta_s \sqrt{\hat{s}}/2$) and the hard region ($E_5 > \delta_s \sqrt{\hat{s}}/2$). The quantity δ_c separates the hard region into the hard collinear (HC) region and hard noncollinear ($\overline{\rm HC}$) region. The criterion for separating the HC region is described as follows: the region for real gluon/light-(anti)quark emission with $\hat{s}_{15}$ (or $\hat{s}_{25}$) $< \delta_c \hat{s}$ (where $\hat{s}_{ij} = (p_i + p_j)^2$) is called the HC region. Otherwise it is called the $\overline{\rm HC}$ region which in our case is related to

$$\begin{aligned} &\gamma(p_1) b(p_2) \to \pi_t^-(p_3) t(p_4) g(p_5), \\ &\gamma(p_1) g(p_2) \to \pi_t^-(p_3) t(p_4) \bar{b}(p_5), \end{aligned} \tag{7}$$

corresponding to real gluon emission and real light-(anti) quark emission partonic processes, respectively. After combining all these contributions, the UV and IR singularities in $\sigma^{\rm total} = \sigma^{\rm Born} + \sigma^{\rm loop} + \sigma^S + \sigma^{\rm HC} + \sigma^{\overline{\rm HC}}$ are exactly canceled. The dependence on the arbitrary small cutoff parameters δ_s and δ_c then vanishes. These cancelations can be verified numerically in our numerical calculations.

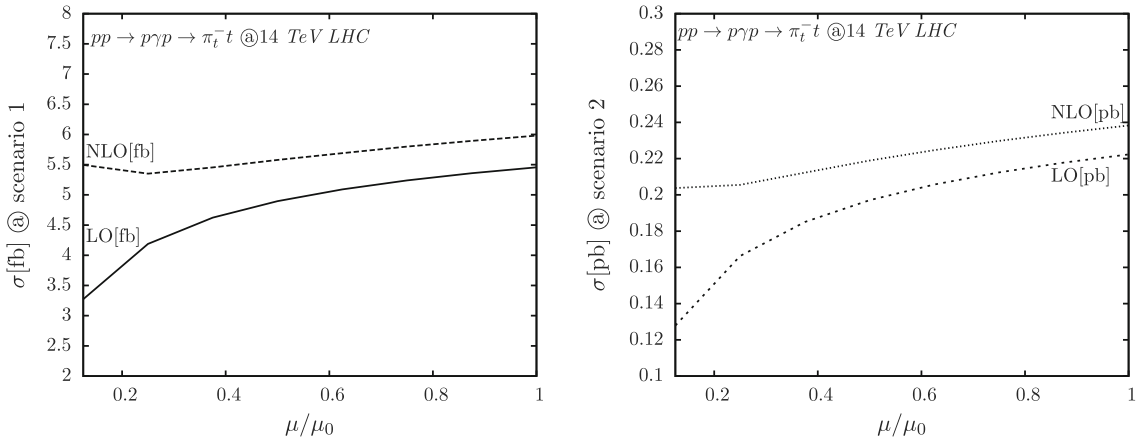

Fig. 4 The scale (μ) dependence of the LO and NLO QCD corrected cross sections for $pp \to p\gamma p \to \pi_t^- t + X$ at $\sqrt{s} = 14$ TeV LHC with $\mu_0 = M_t$, $\delta_s = 10^{-4}$, and $\delta_c = \delta_s/50$. The experimental detector acceptances ($\xi_{\min} < \xi < \xi_{\max}$) are supposed to be $0 < \xi < 1$. *Solid* and *dashed lines* are for scenario 1, LO, and NLO, respectively, while *dotted* and *dot-dotted lines* are for scenario 2, LO, and NLO, respectively

3 Numerical results and discussions

We use FeynArts, FormCalc, and our modified LoopTools (FFL) [62–64] packages to perform the numerical calculation. We use CT10 [65] for the parton distributions for collider physics and BASES [66,67] to do the phase space integration. In the numerical calculations, we take the input as $M_p = 0.938272046$ GeV, $M_Z = 91.1876$ GeV, $M_W = 80.385$ GeV, $M_t = 173.5$ GeV, $\alpha(M_Z^2)^{-1} = 127.918$ [68], $\sqrt{s} = 14$ TeV. For the strong coupling constant $\alpha_s(\mu)$, we use the two-loop evolution of it with the QCD parameter $\Lambda^{n_f=5} = 226$ MeV and get $\alpha_s(\mu_0) = 0.113$. N_f is the number of active flavors. We choose two sets of the parameters related to the TTM model.

- Scenario 1: $M_D = 400$ GeV, $\sin\omega = 0.5$, $M_{W'} = 500$ GeV, $M_{\pi_t} = 400$ GeV;
- Scenario 2: $M_D = 400$ GeV, $\sin\omega = 0.2$, $M_{W'} = 500$ GeV, $M_{\pi_t} = 200$ GeV,

corresponding to high (low) M_{π_t} regions, respectively. The detected acceptances are chosen to be [69,70]:

- ξ_1: CMS-TOTEM forward detectors with $0.0015 < \xi < 0.5$;
- ξ_2: CMS-TOTEM forward detectors with $0.1 < \xi < 0.5$;
- ξ_3: AFP-CMS forward detectors with $0.0015 < \xi < 0.15$.

Before presenting the numerical predictions, several checks should be done. First, The UV and IR safeties are verified numerically after combining all the contributions at the QCD one-loop level. We display random phase space points as well as the cancelation for different divergent parameters with the help of OneLoop [71] to compare with our modified LoopTools. Second, when doing the phase space integration, we use Kaleu [72] to cross check especially for the hard emission contributions. Third, since the total cross section is independent of the soft cutoff $\delta_s (= \Delta E_g/E_b, E_b = \sqrt{\hat{s}}/2)$ and the collinear cutoff δ_c, trivial efforts should be made to check such independence. Fourth, the scale (μ) dependence should be reduced after considering the NLO corrections. Indeed, our results show that the scale uncertainty can be reduced significantly. Choosing the input scenario 1 as an example, if μ varies from $1/8\mu_0$ to $\mu_0 = M_t$, the LO cross section varies from 3.2 to 6 fb, while NLO predictions stay much flatter between 5.5 and 6.4 fb. For more details, see Fig. 4, where we show the scale (μ) dependence of the LO and NLO QCD loop-corrected cross sections for $pp \to p\gamma p \to \pi_t^- t + X$. In the further numerical calculations, we fix $\delta_s = 10^{-4}$, $\delta_c = \delta_s/50$ and choose $\mu = \mu_0 = M_t$.

3.1 Cross sections and distributions

In Fig. 5 we present the cross sections (the left panel) for NLO predictions and the K-factor (the right panel) defined as $\sigma^{\rm NLO}/\sigma^{\rm LO}$ for $pp \to p\gamma p \to \pi_t^- t + X$ as functions of different values of the input parameters in the TTM model. One is $\sin\omega$ and the other is the top-pion mass M_{π_t}. Here we choose the detector acceptance as $0.0015 < \xi < 0.5$. The other parameters related to the TTM model are chosen to be $M_D = 400$ GeV and $M_{W'} = 500$, with $\sin\omega$ varying from 0.2 to 0.8 and M_{π_t} from 200 to 400 GeV, respectively. Our results show that the total LO and NLO cross sections are sensitive to the input parameter $\sin\omega$. When $\sin\omega$ becomes larger, the cross sections reduce obviously. The same behavior can be found for the charged top-pion mass M_{π_t}. When the mass becomes heavier, the phase space of the final states is suppressed, thus leading lower cross sections. The right panel presents the K-factor dependence on $\sin\omega$ and M_{π_t}. No matter how $\sin\omega$ changes, the K-factor does not change much

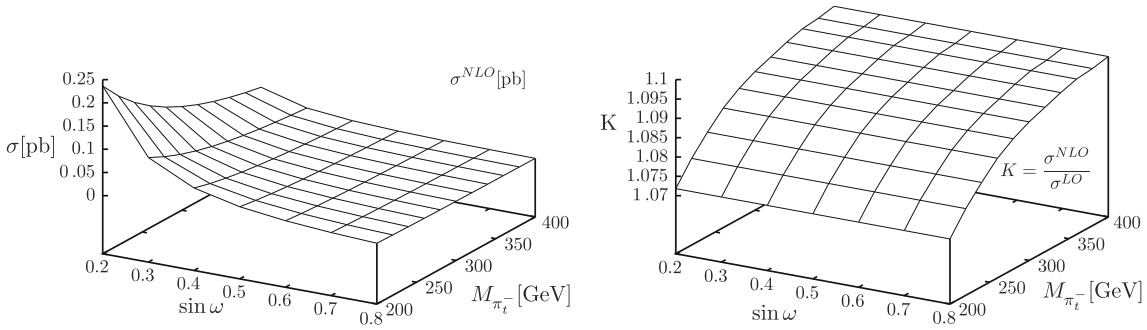

Fig. 5 Cross sections (the *left panel*) for NLO predictions and K-factor (the *right panel*) defined as $\sigma^{\rm NLO}/\sigma^{\rm LO}$ for $pp \to p\gamma p \to \pi_t^- t + X$ as functions of different values of the parameters in TTM models at 14 TeV LHC. Here we choose $0.0015 < \xi < 0.5$. The other parameters related to TTM models are chosen to be $M_D = 400$ GeV, $M_{W'} = 500$, with $\sin\omega$ varying from 0.2 to 0.8 and $M_{\pi_t^-}$ from 200 to 400 GeV, respectively, and the other TTM model input parameters are chosen to be as in scenario 2

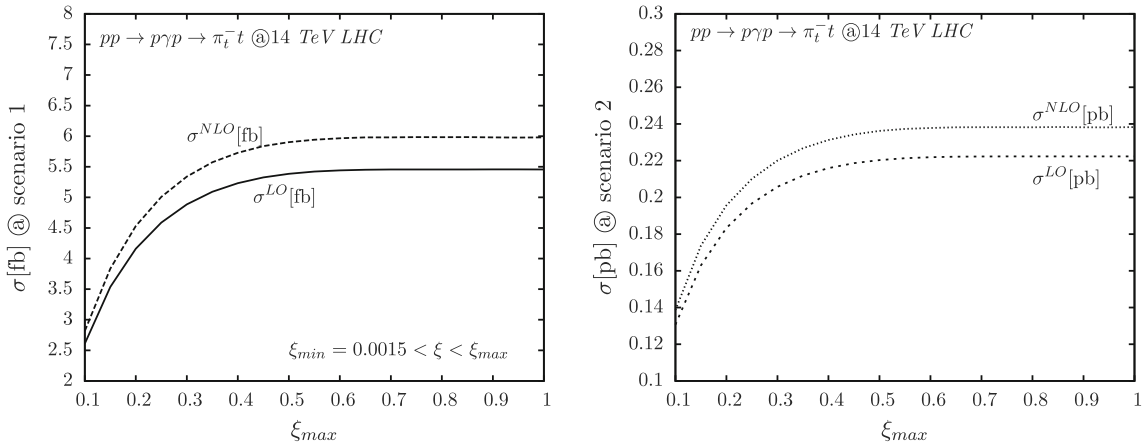

Fig. 6 Cross sections for LO and NLO predictions for $pp \to p\gamma p \to \pi_t^- t + X$ as functions of the different values of the $\xi_{\rm max}$ detector acceptances at the 14 TeV LHC. Here we fix $\xi_{\rm min} = 0.0015$ and take $\xi_{\rm max}$ as a running parameter from 0.15 to 1. The left panel is in units of fb for TTM scenario 1 with *solid* and *dashed lines* for the LO and NLO predictions, while the right axis is in pb for TTM scenario 2 with *dotted* and *dot-dotted lines* for LO and NLO, respectively

with a fixed top-pion mass. While for M_{π_t} becoming larger from 200 to 400 GeV, the K-factor grows up step-by-step, however, not very much, we see, from 1.07 to 1.1, leading to NLO QCD corrections up to around 7−11 % within our chosen parameters.

To see how the cross sections depend on the detector acceptances, in Fig. 6 we fix $\xi_{\rm min} = 0.0015$ and take $\xi_{\rm max}$ as a running parameter. Cross sections for the two input scenarios are presented as $\xi_{\rm max}$ running from 0.15 to 1. The left panel presents results for scenario 1 with dotted and dot-dotted lines for LO and NLO, while the right panel is for scenario 2 with solid and dashed lines for LO and NLO predictions, respectively. From these panels, we can see, for $\xi_{\rm max} < 0.5$, that the cross section enhances rapidly when the ξ acceptances become larger. The case is different for $\xi_{\rm max} > 0.5$ where few contributions contribute. Furthermore, no matter how the detector acceptances change, the ratio of $\sigma^{\rm NLO}$ to $\sigma^{\rm LO}$ does not change much. Typical values of the K-factor equal to 1.09 for scenario 1, and 1.07 for scenario 2 lead to the NLO QCD loop corrections up to 9 and 7 % and keep unchanged as functions of running ξ. However, to avoid misleading ideas, we show Fig. 6 in order to see the dependence on $\xi_{\rm max}$ with fixed $\xi_{\rm min}$. If we change the choice of $\xi_{\rm min}$, for example, from 0.0015 to 0.1, the results, i.e., the cross section of the signal at LO and NLO, the K-factor, will change to other values.

We present the transverse momentum (p_T) and rapidity (y) distributions for the charged top-pion in Fig. 7. For $p_T^{\pi_t^-}$, the NLO predictions can clearly enhance the LO distributions around the peak range and the same behavior can be found for the p_T^t distributions. It will be interesting to see $y^{\pi_t^-}$ where the NLO corrections can shift the LO rapidity obviously in the way of moving the position where $y^{\pi_t^-}$ peaked. Take $0.0015 < \xi < 0.5$ as an example, the distribution $y^{\pi_t^-}$ peaked at $y = -0.18$ for LO while the NLO predictions move the LO $y^{\pi_t^-}$ peak to $y = -0.42$ but there is no obvious enhancement to the LO predictions.

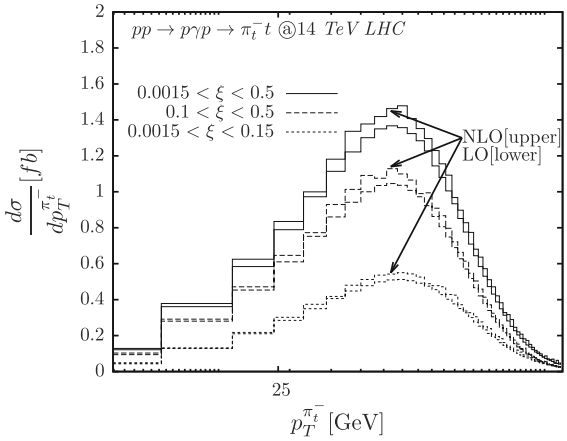

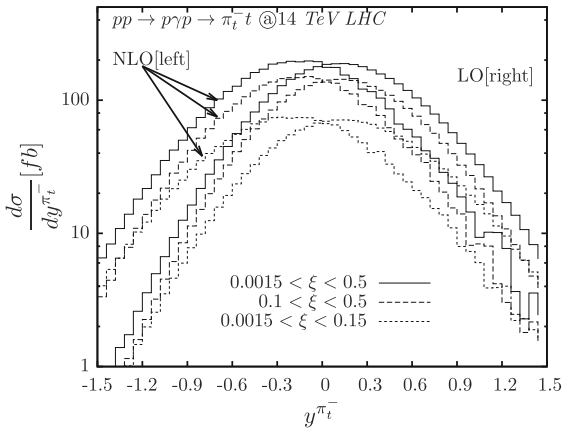

Fig. 7 The LO (*lower curves*) and NLO (*upper curves*) transverse momentum (p_T) and rapidity (y) distributions of the charged top-pion π_t^- for the process $pp \to p\gamma p \to \pi_t^- t + X$ at the 14 TeV LHC. The experimental detector acceptances ($\xi_{\min} < \xi < \xi_{\max}$) are chosen to be $0.0015 < \xi < 0.5$ (*solid lines*), $0.1 < \xi < 0.5$ (*dashed lines*), and $0.0015 < \xi < 0.15$ (*dotted lines*), respectively, and the TTM model input parameters are chosen to be as in scenario 2

3.2 Signal background analysis and parameter sensitivity

Now let us turn to the signal and background analysis. From Ref. [6] we see that, for $M_{h_t} \geq 300$ GeV and $M_{\pi_t} \leq 600$ GeV, the charged top-pions π_t^- dominantly decay into $\bar{t}b$ and we have $Br(\pi_t^- \to \bar{t}b) > 90\,\%$. As for the mass of M_{π_t} to become higher, the validity of this statement is no longer independent of the mass of, for example, the top-Higgs, M_{h_t}. However, for each value of $\sin\omega$, a specific range of masses for the top-Higgs is excluded by the Tevatron data. For example, taking the illustrative value $\sin\omega = 0.5$, the data implies that the mass range $140\,\text{GeV} < M_{H_t} < 195\,\text{GeV}$ is excluded. Here we concentrate on the case where $M_{h_t} \geq 350$ GeV. Even though, as the mass M_{π_t} becomes higher than 600 GeV, the decay mode $\pi^{\pm} \to W^{\pm} H_t$ becomes more and more competitive, where the assumption of a branching ratio $Br(\pi_t^- \to \bar{t}b) < 90\,\%$ should be considered. We concentrate on the $\pi_t^{\pm} \to \bar{t}b(t\bar{b})$ decay modes. In this case, photoproduction of the charged top-pion associated with a top quark can easily be transferred to the $t\bar{t}b$ final state through

$$pp \to p\gamma p \to \pi_t^- t \to \bar{t}bW^+b \to W^-\bar{b}bW^+b \to \ell^+\ell^-\bar{b}bb\not{E}_T \tag{8}$$

and thus gives rise to the $\ell^+\ell^-\bar{b}bb\not{E}_T$ signature via γb collisions at the LHC.

The backgrounds appear in two kinds of processes. The first, called irreducible background, comes from photoproduction with a very similar final state as the signal. The second has the same final state but occurs through different processes induced by partonic interactions and is called a reducible background. The key difference between photoproduction and partonic interactions at the LHC lies in the absence of color exchange on the photon side. This causes an important zone of rapidity to be completely devoid of hadronic activity; it is called a large rapidity gap (LRG) and it is a natural way to distinguish photoproduction and partonic backgrounds. In the framework of EPA, emitted quasi-real photons from the protons have a low virtuality and are scattered with small angles from the beam pipe. Therefore when a proton emits a quasi-real photon it should also be scattered with a small angle. Hence, intact scattered protons exit the central detector without being detected. This causes a decrease in the energy deposit in the corresponding forward region compared to the case in which the proton remnants are detected by the calorimeters. Consequently, for any reaction like $pp \to p\gamma p \to pX$, one of the forward regions of the central detector shows a significant lack of energy. The region with a lack of energy (or equivalently lack of particles) defines a forward LRG. Backgrounds from the usual pp deep inelastic processes can be rejected by applying a selection cut on this quantity.

In addition, another tagging method based on the same physics properties of photoproduction events is to place an exclusivity condition on the reconstructed particle tracks on the gap side which can obviously reduce partonic backgrounds [73]. Even if both conditions are used and the partonic background is reduced to a level that does not allow for proper signal extraction, elastic photon emission can be tagged using a very forward detector (VFD) [74] placed hundreds of meters away from the interaction point. For instance, the case for which VFD stations would be put at 220 and 420 m from the interaction point is mandatory in order to retain low partonic backgrounds [75]. Indeed, when an intact proton is scattered with a large pseudorapidity it escapes detection from the central detectors. But since its energy is

Table 1 The TTM parameters $\sin\omega$ and M_{π_t} sensitivities on the signal background ratio $S/\sqrt{B}$. 5σ for the discovery boundary and 3σ for the excluding boundary. The detector acceptance here is chosen to be $0.0015 < \xi < 0.5$

$\sin\omega$						
M_{π_t} [GeV]	$\mathcal{L} = 1\,fb^{-1}$		$\mathcal{L} = 10\,fb^{-1}$		$\mathcal{L} = 100\,fb^{-1}$	
	5σ	3σ	5σ	3σ	5σ	3σ
300	0.594	0.693	0.800	0.865	0.922	0.950
400	0.450	0.544	0.671	0.761	0.851	0.901
500	0.340	0.422	0.542	0.641	0.757	0.832
600	0.256	0.326	0.431	0.525	0.650	0.742
700	0.181	0.230	0.307	0.385	0.500	0.598
800	0.135	0.171	0.231	0.291	0.387	0.477
900	<0.1	0.130	0.173	0.220	0.292	0.370
1000	<0.1	<0.1	0.131	0.162	0.221	0.281
1100	<0.1	<0.1	<0.1	0.121	0.164	0.207
1200	<0.1	<0.1	<0.1	<0.1	0.122	0.148

lower than the beam energy, its trajectory decouples from the beam path into the very forward region. Forward detectors can detect particles with a large pseudorapidity. The detection of final state intact protons by the forward detectors provides a characteristic signature. Backgrounds from usual DIS processes can also be rejected by use of this characteristic signature provided by the forward detectors.

Therefore in our paper, the considered backgrounds come from protoproduction. Even though in high-energy γp interactions at the LHC, one needs to pay attention to single diffractive (SD) backgrounds. SD backgrounds can most likely be suppressed using AFP and tuned exclusivity cuts. There are not many papers dealing with diffractive photoproduction processes at LHC. Here we use the most powerful cut: the p_T cut of a proton is larger than 100 MeV to suppress the diffraction background from photon-induced processes with the help of Pythia 8 [76] and in-house modifications. After considering the b-tagging efficiency and the rejection factors for the light jets, we get the SD background for our production in about the order of 0.1 fb, which has been taken into our consideration. From this point we can see that the main backgrounds would still come from $t\bar{t}$ plus jet ($t\bar{t}j$) photoproduction. Different from normal pp collision, in γp collisions where photoproduction of top quark pairs has similar cross sections like, for example, $W^- t$ productions, we have only $\sim$1.4 pb [19], while for $t\bar{t}j$, we have roughly $\sim$16 fb after considering the fake b-tagging efficiency, leading to such related background processes going easier than in the case of the pp collision. Here we assume that the $\pi_t^{\pm}$ fully decay to $t\bar{b}(\bar{t}b)$ if $M_{\pi_t} < 600$ GeV, while $Br(\pi_t^{\pm} \to t\bar{b}(\bar{t}b) < 90\,\%)$ [6] should be considered if $M_{\pi_t} \geq 600$ GeV. For the SM gauge bosons $W^{\pm}$ to decay leptonically, $W^{\pm} \to l\nu$, the signal is $S = \mathcal{L} \times \sigma(pp \to prp \to \pi_t^{\pm} t \to t\bar{t}b) \times K^{\mathrm{NLO}} \times [BR(t \to Wb)]^2 \times [3 \times BR(W \to \ell\nu)]^2$, and the corresponding background as $B = \mathcal{L} \times \sigma(pp \to prp \to t\bar{t}j) \times Eff_j \times [BR(t \to Wb)]^2 \times [3 \times BR(W \to \ell\nu)]^2$ with $j = u, d, c, s, b, \bar{u}, \bar{d}, \bar{c}, \bar{s}, \bar{b}, g$ and Eff_j is the fake b-tagging efficiency of the jets. For c-jets and light jets, a fake b-tagging efficiency of 10 and 1 %, respectively, is assumed. Here we take $BR(t \to Wb) \approx 1$ and $BR(W \to \ell\nu) \approx 0.108$. For the luminosity $\mathcal{L}$ we take 1, 10, and 100 fb^{-1}, respectively. In Table 1, we present the parameters' sensitivity on the signal background ratio $S/\sqrt{B}$. Here we choose $0.0015 < \xi < 0.5$. The background cross section after considering all the b-tagging efficiency and the rejection factors for the c, $\bar{c}$, and light jets is 1.68 fb. The 5σ and 3σ bounds of the parameters are presented with three values of the luminosity. For $S/\sqrt{B} > 5$, the new physics signal will be detected obviously while for $S/\sqrt{B} < 3$ it will be a challenge to detect.

Our results show that, for low M_{π_t}, the $\sin\omega$ discovery range is larger than the case of high M_{π_t}. As the top-pion mass becomes larger, the $\sin\omega$ discovery range is suppressed. When $M_{\pi_t} > 900$ GeV, the heavy final state strongly suppresses the phase space. The signal becomes much smaller and makes it more a challenge to detect. In this case, a higher luminosity is needed to make the detection possible and push the discovery boundary larger. Two ways can be used in order to constrain the parameters or the excluding boundary more strictly: one is, as we see, to enhance the luminosity which can expand the related parameter space, see Table 1, while the other one is to take more kinematical cuts to improve the ratio $S/\sqrt{B}$. In our case for example, if a p_T^{jet} cut is taken to be larger than 200 GeV, this can strongly suppress the ttj backgrounds and thus lead to better $S/\sqrt{B}$ in parts of the TTM parameter space.

4 Summary

In this work, we present the precise photoproduced charged top-pion $\pi_t^{\pm}$ production associated with a top through $pp \to p\gamma p \to \pi_t^{\pm} t + X$ at the 14 TeV LHC at NLO QCD loop level. We find that the cross sections are sensitive to the TTM parameters, and the smaller the $\sin\omega$ is or the lighter the top-pion π_t^{-} is, the larger the cross sections will be. The typical QCD correction value is $7-11$ %, which does not depend much on the TTM parameter $\sin\omega$ as well as the detector acceptances ξ. We also present the 5σ discovery and 3σ excluding boundaries as functions of the TTM parameters for three values of the luminosity at the future LHC.

Acknowledgments Sun Hao thanks Dr. Inanc Sahin for being kind enough to provide invaluable advice. Project supported by the National Natural Science Foundation of China (No. 11205070, 11275088), Shandong Province Natural Science Foundation (No. ZR2012AQ017), Natural Science Foundation of the Liaoning Scientific Committee (No. 201102114), Foundation of Liaoning Educational Committee (No. LT2011015) and by the Fundamental Research Funds for the Central Universities (No. DUT13RC(3)30).

References

1. C.T. Hill, Phys. Lett. B **345**, 483 (1995)
2. K.D. Lane, E. Eichten, Phys. Lett. B **352**, 382 (1995)
3. K.D. Lane, Phys. Lett. B **433**, 96 (1998)
4. C. Csaki, C. Grojean, H. Murayama, L. Pilo, J. Terning, Phys. Rev. D **69**, 055006 (2004)
5. R.S. Chivukula, N.D. Christensen, B. Coleppa, E.H. Simmons, Phys. Rev. D **80**, 035011 (2009)
6. R.S. Chivukula, E.H. Simmons, B. Coleppa, H.E. Logan, A. Martin, Phys. Rev. D **83**, 055013 (2011)
7. R.S. Chivukula, P. Ittisamai, E.H. Simmons, B. Coleppa, H.E. Logan, A. Martin, J. Ren, Phys. Rev. D **86**, 095017 (2012)
8. A. Abulencia et al. (CDF Collaboration), Phys. Rev. Lett. **98**, 112001 (2007)
9. T. Aaltonen et al. (CDF Collaboration), Phys. Rev. Lett. **102**, 222002 (2009)
10. T. Aaltonen et al. (CDF Collaboration), Phys. Rev. Lett. **99**, 242002 (2007)
11. T. Aaltonen et al. (CDF Run II Collaboration), Phys. Rev. D **77**, 052004 (2008)
12. T. Aaltonen et al. (CDF Collaboration), Phys. Rev. Lett. **102**, 242001 (2009)
13. M. Tasevsky, Diffractive physics program in ATLAS experiment. Nucl. Phys. Proc. Suppl. **179–180**, 187–195 (2008)
14. M. Tasevsky, Measuring central exclusive processes at LHC. arXiv:0910.5205
15. C. Royon, (RP220 Collaboration), Project to install roman pot detectors at 220 m in ATLAS. arXiv:0706.1796
16. M.G. Albrow et al., FP420: An R&D proposal to investigate the feasibility of installing proton tagging detectors in the 420-m region at LHC, CERN-LHCC-2005-025 (2005)
17. B.E. Cox, (FP420 R and D Collaboration), The FP420 R&D Project at the LHC. arXiv:hep-ph/0609209
18. C. Royon, The ATLAS forward physics project. arXiv:1302.0623
19. J. de Favereau de Jeneret, V. Lemaitre, Y. Liu, S. Ovyn, T. Pierzchala, K. Piotrzkowski, X. Rouby, N. Schul, M. Vander Donckt, High energy photon interactions at the LHC. arXiv:0908.2020
20. S. Ovyn, Associated W and Higgs boson photoproduction and other electroweak photon induced processes at the LHC. Nucl. Phys. Proc. Suppl. **179–180**, 269–276 (2008). arXiv:0806.1157
21. S. Ovyn, J. de Favereau de Jeneret, High energy single top photoproduction at the LHC. arXiv:0806.4841
22. J. de Favereau de Jeneret, S. Ovyn, Single top quark photoproduction at the LHC. Nucl. Phys. Proc. Suppl. **179–180**, 277–284 (2008). arXiv:0806.4886
23. N. Schul, K. Piotrzkowski, Detection of two-photon exclusive production of supersymmetric pairs at the LHC. Nucl. Phys. Proc. Suppl. **179–180**, 289–297 (2008). arXiv:0806.1097
24. K. Piotrzkowski, N. Schul, Two-photon exclusive production of supersymmetric pairs at the LHC. AIP Conf. Proc. **1200**, 434–437 (2010). arXiv:0910.0202
25. S. Heinemeyer, V.A. Khoze, M.G. Ryskin, W.J. Stirling, M. Tasevsky, G. Weiglein, Studying the MSSM Higgs sector by forward proton tagging at the LHC. Eur. Phys. J. C **53**, 231–256 (2008). arXiv:0708.3052
26. S. Heinemeyer, V.A. Khoze, M.G. Ryskin, W.J. Stirling, M. Tasevsky, G. Weiglein, Central exclusive diffractive MSSM Higgs-Boson production at the LHC. J. Phys. Conf. Ser. **110**, 072016 (2008). arXiv:0801.1974
27. S. Heinemeyer, V.A. Khoze, M.G. Ryskin, M. Tasevsky, G. Weiglein, BSM Higgs physics in the exclusive forward proton mode at the LHC. Eur. Phys. J. C **71**, 1649 (2011). arXiv:1012.5007
28. M. Tasevsky, Exclusive MSSM, Higgs production at the LHC after Run I. Eur. Phys. J. C **73**, 2672 (2013). arXiv:1309.7772
29. S. Atag, S.C. Inan, I. Sahin, Extra dimensions in photon-induced two lepton final states at the CERN-LHC. Phys. Rev. D **80**, 075009 (2009). arXiv:0904.2687
30. S. Atag, S.C. Inan, I. Sahin, Extra dimensions in $\gamma\gamma \to \gamma\gamma$ process at the CERN-LHC. JHEP **09**, 042 (2010). arXiv:1005.4792
31. I. Sahin, A.A. Billur, S.C. Inan, B. Sahin, M. Koksal, P. Tektas, E. Alici, R. Yildirim, Probe of extra dimensions in γ q $\to \gamma$ q at the LHC. Phys. Rev. D **88**, 095016 (2013). arXiv:1304.5737
32. I. Sahin, S.C. Inan, Probe of unparticles at the LHC in exclusive two lepton and two photon production via photon–photon fusion. JHEP **0909**, 069 (2009). arXiv:0907.3290
33. T. Pierzcha la, K. Piotrzkowski, Sensitivity to anomalous quartic gauge couplings in photon–photon interactions at the LHC. Nucl. Phys. Proc. Suppl. **179–180**, 257–264 (2008). arXiv:0807.1121
34. O. Kepka, C. Royon, Anomalous WW_γ coupling in photon-induced processes using forward detectors at the CERN LHC. Phys. Rev. D **78**, 073005 (2008). arXiv:0808.0322
35. C. Royon, E. Chapon, O. Kepka, Anomalous trilinear and quartic WWγ, WW$\gamma\gamma$, ZZγ and ZZ$\gamma\gamma$ couplings in photon induced processes at the LHC. PoS EPS-HEP2009 (2009) 380. arXiv:0909.5237
36. E. Chapon, C. Royon, O. Kepka, Anomalous quartic $WW_{\gamma\gamma}$, $ZZ_{\gamma\gamma}$, and trilinear WW_γ couplings in two-photon processes at high luminosity at the LHC. Phys. Rev. D **81**, 074003 (2010). arXiv:0912.5161
37. I. Sahin, A.A. Billur, Anomalous WW_γ couplings in γ–proton collision at the LHC. Phys. Rev. D **83**, 035011 (2011). arXiv:1101.4998
38. R.S. Gupta, Probing quartic neutral gauge boson couplings using diffractive photon fusion at the LHC. Phys. Rev. D **85**, 014006 (2012). arXiv:1111.3354

39. I. Sahin, B. Sahin, Anomalous quartic $ZZ_{\gamma\gamma}$ couplings in γproton collision at the LHC. Phys. Rev. D **86**, 115001 (2012). arXiv:1211.3100
40. A. Senol, ZZ_{γ} and $Z_{\gamma\gamma}$ anomalous couplings in γp collision at the LHC. Phys. Rev. D **87**, 073003 (2013). arXiv:1301.6914
41. A. Senol, Anomalous quartic $WW_{\gamma\gamma}$ and $ZZ_{\gamma\gamma}$ couplings in γp collision at the LHC. arXiv:1311.1370
42. S. Fichet, G. von Gersdorff, O. Kepka, B. Lenzi, C. Royon, M. Saimpert, Probing new physics in diphoton production with proton tagging at the Large Hadron Collider. arXiv:1312.5153
43. I. Sahin, M. Koksal, Search for electromagnetic properties of the neutrinos at the LHC. JHEP **1103**, 100 (2011). arXiv:1010.3434
44. S. Atag, A.A. Billur, Possibility of determining τ lepton electromagnetic moments in $\gamma\gamma \to \tau^+\tau^-$ process at the CERN-LHC. JHEP **1011**, 060 (2010). arXiv:1005.2841
45. I. Sahin, Electromagnetic properties of the neutrinos in gamma-proton collision at the LHC. Phys. Rev. D **85**, 033002 (2012). arXiv:1201.4364
46. M. Köksal, S.C. Inan, Anomalous $tq\gamma$ couplings in γp collision at the LHC. arXiv:1305.7096
47. B. Sahin, A.A. Billur, Anomalous Wtb couplings in gamma-proton collision at the LHC. Phys. Rev. D **86**, 074026 (2012). arXiv:1210.3235
48. H. Sun, Probe anomalous $tq\gamma$ couplings through single top photoproduction at the LHC. arXiv:1402.1817
49. M. Chaichian, P. Hoyer, K. Huitu, V.A. Khoze, A.D. Pilkington, Searching for the triplet Higgs sector via central exclusive production at the LHC. JHEP **0905**, 011 (2009). arXiv:0901.3746
50. C.-X. Yue, H.-J. Zong, S.-Z. Wang, Phys. Lett. B **575**, 25 (2003)
51. G.-L. Liu, Phys. Rev. D **82**, 115032 (2010)
52. C.-X. Yue, J. Guo, J. Zhang, Q.-G. Zeng, Commun. Theor. Phys. **58**, 711 (2012)
53. T. Plehn, Phys. Rev. D **67**, 014018 (2003)
54. R.S. Chivukula, B. Coleppa, S. Di Chiara, E.H. Simmons, H.-J. He, M. Kurachi, M. Tanabashi, Phys. Rev. D **74**, 075011 (2006)
55. G. Cvetic, Rev. Mod. Phys. **71**, 513 (1999)
56. C.T. Hill, E.H. Simmons, Phys. Rept. **381**, 235 (2003). [Erratum-ibid **390**, 553 (2004)]
57. R.S. Chivukula, E.H. Simmons, B. Coleppa, H.E. Logan, A. Martin, Phys. Rev. D **84**, 095022 (2011)
58. V.M. Budnev, I.F. Ginzburg, G.V. Meledin, V.G. Serbo, Phys. Rep. **15**, 181 (1975)
59. G. Baur, K. Hencken, D. Trautmann, S. Sadowsky, Y. Kharlov, Phys. Rep. **364**, 359 (2002)
60. K. Piotrzkowski, Phys. Rev. D **63**, 071502 (2001). hep-ex/0009065
61. B.W. Harris, J.F. Owens, Phys. Rev. D **65**, 094032 (2002)
62. T. Hahn, Comput. Phys. Commun. **140**, 418–431 (2001)
63. T. Hahn, Nucl. Phys. Proc. Suppl. **89**, 231–236 (2000)
64. T. Hahn, M. Perez-Victoria, Comput. Phys. Commun. **118**, 153–165 (1999)
65. M. Guzzi, P. Nadolsky, E. Berger, H.-L. Lai, F. Olness, C.-P. Yuan, SMU-HEP-10-11. arXiv:1101.0561
66. S. Kawabata, Comp. Phys. Commun. **88**, 309 (1995)
67. F. Yuasa, D. Perret-Gallix, S. Kawabata, T. Ishikawa, Nucl. Instrum. Methods A **389**, 77 (1997)
68. J. Beringer et al., Particle Data Group, Phys. Rev. D **86**, 010001 (2012)
69. M.G. Albrow et al. (FP420 R and D Collaboration), arXiv:0806.0302
70. V. Avati, K. Osterberg, Acceptance calculations methods for low-beta optics, Report No. CERN-TOTEM-NOTE-2005-002 (2006)
71. A. van Hameren, Comput. Phys. Commun. **182**, 2427–2438 (2011)
72. A. van Hameren, arXiv:1003.4953
73. J. de Favereau, S. de Jeneret, Ovyn, Nucl. Phys. Proc. Suppl. **179–180**, 277–284 (2008)
74. X. Rouby, Nucl. Phys. Proc. Suppl. **179–180**, 202–210 (2008)
75. S. Ovyn, Nucl. Phys. Proc. Suppl. **179–180**, 269–276 (2008)
76. T. Sjöstrand, S. Mrenna, P. Skands, A brief introduction to PYTHIA 8.1. Comput. Phys. Comm. **178**, 852 (2008). arXiv:0710.3820